The visibility of Lyman α emitters during reionization

Pratika Dayal,[1]⋆ Antonella Maselli[2] and Andrea Ferrara[3]

[1] *SISSA/International School for Advanced Studies, Via Bonomea 265, 34136 Trieste, Italy*
[2] *Osservatorio Astrofisico di Arcetri, Largo Enrico Fermi 5, 50125 Firenze, Italy*
[3] *Scuola Normale Superiore, Piazza dei Cavalieri 7, 56126 Pisa, Italy*

ABSTRACT

We present the first Lyman α emitter (LAE) study that combines: (i) cosmological smoothed particle hydrodynamic (SPH) simulations run using GADGET-2, (ii) radiative transfer simulations (CRASH) and (iii) a previously developed LAE model. This complete LAE model accounts for the intrinsic LAE, Lyα/continuum luminosity, dust enrichment and Lyα transmission through the intergalactic medium (IGM) to quantify the effects of reionization, dust and velocity fields on the Lyα and UV luminosity functions (LFs). We find that a model neglecting dust sorely fails to reproduce either the slope or the magnitude of the observed Lyα and UV LFs. Clumped dust is required to simultaneously fit the observed UV and Lyα LFs, such that the intrinsic Lyα-to-continuum luminosity is enhanced by a factor $f_\alpha/f_c \sim 1.5$ (3.7) excluding (including) peculiar velocities. The higher value including velocity fields arises since LAEs reside in large potential wells and inflows decrease their Lyα transmission. For the first time, a *degeneracy* is found between the ionization state of the IGM and the clumping of dust inside high-redshift galaxies. The Lyα LF $z \sim 5.7$ can be well reproduced (to within a 5σ error) by a wide range of IGM average neutral hydrogen fraction, $3.4 \times 10^{-3} < \langle \chi_{\rm H\,I} \rangle < 0.16$, provided that the increase in the Lyα transmission through a more ionized IGM is compensated by a decrease in the Lyα escape fraction from the galaxy due to dust absorption. The physical properties of LAEs are presented along with a discussion of the assumptions adopted.

Key words: radiative transfer – methods: numerical – dust, extinction – galaxies: high-redshift – galaxies: luminosity function, mass function – cosmology: theory.

1 INTRODUCTION

The epoch of reionization marks the second major change in the ionization state of the Universe. Reionization begins when the first sources of neutral hydrogen (H I) ionizing photons form within dark matter potential wells and start building an ionization region around themselves, the so-called Strömgren sphere. However, the reionization history and the redshift at which it ends still remain the subject of much discussion. This is because the reionization process depends on a number of parameters including the initial mass function (IMF) of the first sources, their star formation rates (SFR), their stellar metallicity and age, the escape fraction of H I ionizing photons produced by each source and the clumping of the intergalactic medium (IGM), to name a few.

Given the large number of free parameters that inevitably enter into the construction of theoretical reionization models, it is imperative to compare and update the models as fresh data sets are acquired. In this sense, it has been suggested (Malhotra & Rhoads

2004; Santos 2004; Mesinger, Haiman & Cen 2004; Malhotra & Rhoads 2005; Haiman & Cen 2005; Dijkstra, Lidz & Wyithe 2007; Mesinger & Furlanetto 2008; Dayal, Ferrara & Gallerani 2008; Dayal et al. 2009; Dayal, Ferrara & Saro 2010) that a class of high-redshift galaxies called Lyman α emitters (LAEs) could be an important addition to complementary data sets to constrain the reionization history.

LAEs, galaxies identified by means of their very strong Lyα line (1216 Å) emission, have been becoming increasingly popular as probes of reionization for three primary reasons. First, specific signatures like the strength, width and the continuum break blue-wards of the Lyα line make the detection of LAEs unambiguous to a large degree. Secondly, since Lyα photons have a large absorption cross-section against H I, their attenuation can be used to put constraints on the ionization state of the IGM. Thirdly, there are hundreds of confirmed LAEs at $z \sim 4.5$ (Finkelstein et al. 2007), $z \sim 5.7$ (Malhotra et al. 2005; Shimasaku et al. 2006) and $z \sim 6.6$ (Taniguchi et al. 2005; Kashikawa et al. 2006), which exactly probe the redshift range around which reionization is supposed to have ended.

The data accumulated on LAEs show some very surprising features; while the apparent Lyα luminosity function (LF) does not

⋆E-mail: dayal@sissa.it

show any evolution between $z = 3.1$ and 5.7 (Ouchi et al. 2008), it changes appreciably between $z = 5.7$ and 6.6, with L_* (the luminosity of the break, after which the number density decreases rapidly) at $z = 6.6$ (Kashikawa et al. 2006) being about 50 per cent of the value at $z = 5.7$ (Shimasaku et al. 2006). Unexpectedly, however, the ultraviolet (UV) LF does not show any evolution between these same redshifts. Although Kashikawa et al. (2006) have proposed this evolution in the Lyα LF to be indicative of a sudden change in the ionization state of the IGM, the problem of why reionization would affect the high-luminosity tail of the Lyα LF rather than the faint end, as expected, remains.

In spite of a number of diverse approaches, the effects of the ionization state of the IGM on the visibility of LAEs still remain poorly understood. This is primarily because understanding/constraining the ionization state of the IGM using LAEs requires: (i) a detailed knowledge of the physical properties of each galaxy, including the SFR, stellar age and stellar metallicity, needed to calculate the intrinsic Lyα and continuum luminosity produced by stellar sources; (ii) the intrinsic Lyα and continuum luminosity produced by the cooling of collisionally excited H I in the interstellar medium (ISM); (iii) an understanding of the dust formation, enrichment and distribution in each galaxy, necessary to calculate the fractions of escaping Lyα and continuum photons and (iv) a full radiative transfer (RT) calculation to obtain the fraction of Lyα luminosity transmitted through the IGM for each galaxy.

Although a number of simulations have been used in the past to study LAEs, they lack one or more of the aforementioned ingredients. Since they used an *N*-body simulation, McQuinn et al. (2007) were forced to neglect the intrinsic properties of the galaxies and their dust enrichment, although they carried out analytic RT. Iliev et al. (2008) used a simulation that only followed dark matter; they also could not use the intrinsic galaxy properties or calculate the dust enrichment, although they carried out a complete RT calculation. Nagamine et al. (2008) used a smoothed particle hydrodynamics (SPH) simulation to obtain the intrinsic SFR for each galaxy; however, they did not calculate the dust enrichment and assumed a fixed value of the IGM transmission, ignoring RT. Dayal et al. (2009, 2010) used an SPH simulation and the intrinsic galaxy properties to calculate the luminosity from both stellar sources and cooling of H I, calculated the dust enrichment and the IGM transmission; the only missing ingredient in their work was the RT calculation. Most recently, Zheng et al. (2010) have carried out an RT calculation on an SPH simulation; however, they have not included any dust calculation or the luminosity contribution from the cooling of H I.

Our aim in this work is to build a LAE model containing all these ingredients, so as to determine the relative importance of dust, peculiar velocity fields and patchy reionization, in shaping the observed Lyα and UV LFs. We start with an introduction to the SPH and RT simulations used in Section 2. We then present the main ingredients of our LAE model, including the calculation of the intrinsic luminosity from stellar sources/cooling of H I, the dust enrichment and the IGM transmission, in Section 3. Once the model is laid down, we present the results obtained with it and quantify the relative importance of dust, peculiar velocities and reionization on the Lyα and UV LFs in Section 4. The physical properties of the galaxies identified as LAEs are shown in Section 5. We conclude by mentioning the caveats and shortcomings of our model in Section 6. The simulations used in this work are based on a Λ cold dark matter (ΛCDM) cosmological model with $\Omega_\Lambda = 0.7$, $\Omega_b = 0.3$, $\Omega_m = 0.04$, $H = 100\,h\,\mathrm{km\,s^{-1}\,Mpc^{-1}}$, where $h = 0.7$ and a scale invariant power spectrum of the initial density perturbations is normalized to $\sigma_8 = 0.9$.

2 HYDRO AND RADIATIVE TRANSFER

The Lyα and UV LFs presented in this work are based on the results from combined runs of SPH and RT simulations, carried out using GADGET-2 (Springel 2005)[1] and CRASH (Maselli, Ferrara & Ciardi 2003; Maselli, Ciardi & Kanekar 2009), respectively, which are coupled to a previously developed LAE model (Dayal et al. 2008, 2009, 2010). GADGET-2 generates the redshift evolution of the density field, the baryonic density distribution and the velocity fields in a $100\,h^{-1}$ Mpc comoving volume; we obtain a snapshot of the simulation at $z \sim 6.1$. The specific simulation used in this work is the G5 run described in Springel & Herquist (2003), which is part of an accurate study focused on modelling the star formation history of the Universe. It must be mentioned that Furlanetto et al. (2005) have also used the G5 runs to study the Lyα emission expected from structures, including that from optically thin/self-shielded gas clouds and from star formation, and studied the effects of winds on the Lyα emission at $z = 3$. We refer the reader to this paper for more details.

We have chosen the G5 run since it contains several physical ingredients necessary for our investigation. First, the volume is large enough so that cosmic variance is minimized in the determination of the LFs. Secondly, the SFR ($\dot{M}_*$) is self-consistently inferred from physically motivated prescriptions that convert gas particles into stellar particles and properly take account of the mechanical/chemical feedback associated with supernovae and galactic winds. This point is particularly relevant since the intrinsic luminosity of the galaxies, both in the Lyα and in UV, depends sensitively on $\dot{M}_*$. Also, since the physics governing star formation and galaxy evolution is modelled accurately, the simulation gives us a reliable representation of the galaxy population. As expected, the large simulation volume naturally leads to a relatively coarse mass resolution with the resolution mass being $2.12 \times 10^9\,\mathrm{M_\odot}$ ($3.26 \times 10^8\,\mathrm{M_\odot}$) for dark matter (gas particles). Running a friends-of-friends (FOF) algorithm on the SPH particle distribution, we identify galaxies and obtain their intrinsic properties, including $\dot{M}_*$, the mass-weighted stellar metallicity (Z_*), the total gas and stellar masses. These are then used to calculate the intrinsic Lyα/continuum luminosity, the dust enrichment and the escape fraction of continuum/Lyα photons from the galaxy. All these are presented and discussed in greater detail in Sections 3 and 4.

The RT calculations have been carried out by post-processing the GADGET-2 SPH snapshot at $z \sim 6.1$ using the CRASH code. CRASH is a 3D, grid-based algorithm which combines ray tracing and Monte Carlo sampling techniques to describe the propagation of ionizing radiation through an arbitrary distribution of hydrogen/helium gas and to follow the evolution of the gas properties affected by the matter-radiation interactions, i.e. ionization fractions and temperature. The algorithm implementation is fully described in Maselli et al. (2003, 2009), and we refer interested readers to these works for complete details. In order to use the SPH GADGET-2 outputs as inputs for the gas distribution in space, we need to map the SPH particles on to a grid; for this work we have chosen a 128^3 grid, resulting in a spatial resolution of $0.78\,h^{-1}$ comoving Mpc. Although this degrades the original SPH spatial resolution, it allows feasible computational times for the RT simulations. The main assumptions made for running CRASH are now explained: (i) using RT codes coupled with the Q5 ($10\,h^{-1}$ Mpc) run (see Springel & Herquist 2003), Sokasian, Abel & Hernquist (2003) studied the effects of

---

[1] http://www.mpa-garching.mpg.de/gadget/

small sources ($10^9\,M_\odot$) on reionization. They found that including these sources, they required $f_{esc} = 0.2$ for reionization to end at $z \sim$ 7–8. They also showed that if these small sources are neglected, the number of H I ionizing photons required scales up by about 60 per cent. However, precisely because we do not resolve galaxies below $10^9\,M_\odot$, we initially assume, at $z \sim 6.1$, the gas to be in photoionization equilibrium with a uniform ultraviolet background (UVB) produced by sources below the simulation resolution scale, corresponding to an average neutral hydrogen fraction, $\langle \chi_{H I} \rangle = 0.3$, (ii) we assume that galaxies have formed stars in the past at an average rate $\dot{M}_*$, equal to the one derived at $z \sim 6.1$ and (iii) since the RT simulation is carried out on a SPH snapshot which contains about 2500 galaxies, to reduce the computational running time, we run the RT calculation in the monochromatic mode, with $h\nu = 13.665$ eV. This is a reasonable assumption since the Lyα LFs depend mostly on the average ionization fraction and on the 3D topology of the fully ionized regions; we are therefore not interested in the detailed profiles of the ionization front or a highly accurate estimate of the IGM temperature to probe which of the ionizing radiation of each galaxy would have to be computed from its spectrum.

We briefly digress here to discuss our assumption that galaxies have formed stars in the past at an average rate $\dot{M}_*$, equal to the one derived at $z \sim 6.1$. Although the cosmic SFR density declines towards higher redshifts (see Bouwens et al. 2009), this is because (i) the mass function shifts to lower masses with increasing redshifts, i.e. the number density of large galaxies decreases with increasing redshift, and (ii) smaller galaxies have smaller SFRs. However, the SFR of any single object can very well remain almost constant over a period of about 100–200 Myr, something which is in line with the SED interpretation of the most distant drop-out galaxies. However, we aim to explore the effects of time varying SFR histories in future works.

The specific photoionization rate is calculated using the expression given in equation (12) of Dayal et al. (2008) and then averaging this value over Z_* and stellar ages (t_*) of the galaxies in the SPH simulation. The contribution from all the galaxies determined under the above-mentioned assumptions is then super-imposed on the average UVB value. Finally, we use $f_{esc} = 0.02$ (Gnedin, Kravtsov & Chen 2008) as a characteristic value of the escape fraction of H I ionizing photons from each galaxy. The total ionizing radiation field, which is the sum of that produced by all galaxies identified in the simulation and the UVB, is then evolved with CRASH up to the Hubble time corresponding to $z \sim 6.1$. However, as we are interested in assessing the visibility of LAE as a function of the mean ionization fraction which could correspond to different epochs along any assigned reionization history, no particular meaning should be attached to the redshift parameter.

We digress here to stress the uncertainties in our knowledge of f_{esc}. Although f_{esc} hugely impacts the reionization history, and even though an enormous amount of work has been put into its calculation by various groups, its value remains largely debated. Ricotti & Shull (2000) found $f_{esc} \geq 0.1$ only for haloes of total mass $\leq 10^7\,M_\odot$ at $z \geq 6$, with the value dropping sharply with increasing halo mass. Using ZEUS-3D simulations, Fujita et al. (2003) found $f_{esc} \leq 0.1$ from discs or dwarf starburst galaxies with total mass $\sim 10^{8-10}\,M_\odot$. While Razumov & Sommer-Larsen (2006) concluded that $f_{esc} = 0.01$–0.1 in several young galaxies with $M_{vir} = 10^{12-13}\,M_\odot$ at $z \sim$ 3, in a recent paper, Razumov & Sommer-Larsen (2010) find $f_{esc} \sim 0.8$–0.1 for galaxies of halo mass $\sim 10^{9-11.5}\,M_\odot$. Using detailed hydrodynamic simulations with RT, Gnedin et al. (2008) found $f_{esc} = 0.01$–0.03 for galaxies with mass $\geq 10^{11}\,M_\odot$ at $z \sim 3$–5. Using high-resolution adaptive mesh refinement simulations, Wise & Cen

(2009) have found $f_{esc} = 0.25$–0.8 for dwarf galaxies between $3 \times 10^{6-9}\,M_\odot$. Finally, using RT and SPH simulations, Yajima, Choi & Nagamine (2010) find f_{esc} decreases from ~ 0.4 to ~ 0.07 as the halo mass increases from 10^9 to $10^{11}\,M_\odot$ at $z \sim 3$–6.

As mentioned above, for this work, we adopt a fiducial value of $f_{esc} = 0.02$, based on the results of Gnedin et al. (2008), since a complete modelling of f_{esc} is much beyond of the scope of this paper. Although it is clear that varying the value of f_{esc} would indeed affect the progression of reionization within the box, thereby affecting the visibility of LAEs, as will be shown in Section 4, this problem is alleviated by a degeneracy between the fraction of Lyα photons that escape the galaxy (undamped by dust) and the fraction transmitted through the IGM, as shown in Section 4.4 (discussion in Section 6).

We now return to the results obtained by the CRASH runs. In Fig. 1, we show maps of the H I fraction across a 2D cut through the RT simulation box, at different simulation times. This time sequence then represents a time-line of the reionization process, due to the galaxy population present within the box. Though an approximation, this description catches many of the important features of the reionization process, including the complex topology produced by the inhomogeneities in the density field, by the galaxy properties and by their spatial distribution. The main aim of this work is to study how the visibility of LAEs ($z \sim 6.1$ here) changes as the ionization field they are embedded in evolves from being highly neutral ($\langle \chi_{H I} \rangle = 0.3$) to completely ionized ($\langle \chi_{H I} \rangle \sim 3 \times 10^{-3}$). This requires using a single galaxy population, as obtained from the GADGET-2 snapshot and only evolving the ionization field; if the galaxy population itself were to change, it would not be possible to disentangle the effects of reionization from the effects of galaxy evolution.

Fig. 1 clearly shows the reionization process in its main three phases. First, isolated ionized hydrogen (H II) regions start growing around point sources which are preferentially located along the over-dense filaments of matter. In this stage the size of the isolated H II regions grows differentially according to the production rate of H I ionizing photons from the specific source; the few galaxies with large $\dot{M}_*$ (e.g. the largest galaxy located at the centre having $\dot{M}_* \sim 726\,M_\odot\,yr^{-1}$) can build an ionized region of about 20 Mpc, in a time as short as 10 Myr (see upper-left panel), which grows at a very fast rate due to the vigorous H I ionizing photon output. If observed at the same evolutionary time-scale, due to the smaller H I ionizing photon budget, the H II regions of smaller galaxies are confined to sizes of the order of a few Mpc (< 4 Mpc), which grow slowly. After 10 Myr of continuous star formation activity, the average neutral hydrogen fraction decreases only to $\langle \chi_{H I} \rangle \sim 0.295$. At this early stage, galaxies with $\dot{M}_* \leq 25\,M_\odot\,yr^{-1}$ transmit only about 20 per cent of their Lyα luminosity through the IGM. Consequently, the low-luminosity end of the LF is depressed with respect to the intrinsic emissivity of these sources. On the other hand, galaxies with larger $\dot{M}_*$ are able to transmit a larger amount (~ 30 per cent) of their luminosity through the IGM.

As the H I ionizing photon production from galaxies continues, the sizes of the H II regions increase with time. At about 100 Myr (upper-right panel), the isolated H II regions start overlapping, resulting in an enhancement of the local photoionization rate close to the smaller sources. This allows the ionized regions associated with the latter to grow faster, and results in the build-up of large H II regions also around smaller galaxies. This results in an enhancement in the transmission of the Lyα luminosity for these sources, such that this value increases to ~ 40 per cent, consequently leading to a boost of the low-luminosity end of the Lyα LF. As expected, the overlap phase speeds up the reionization process; for a star
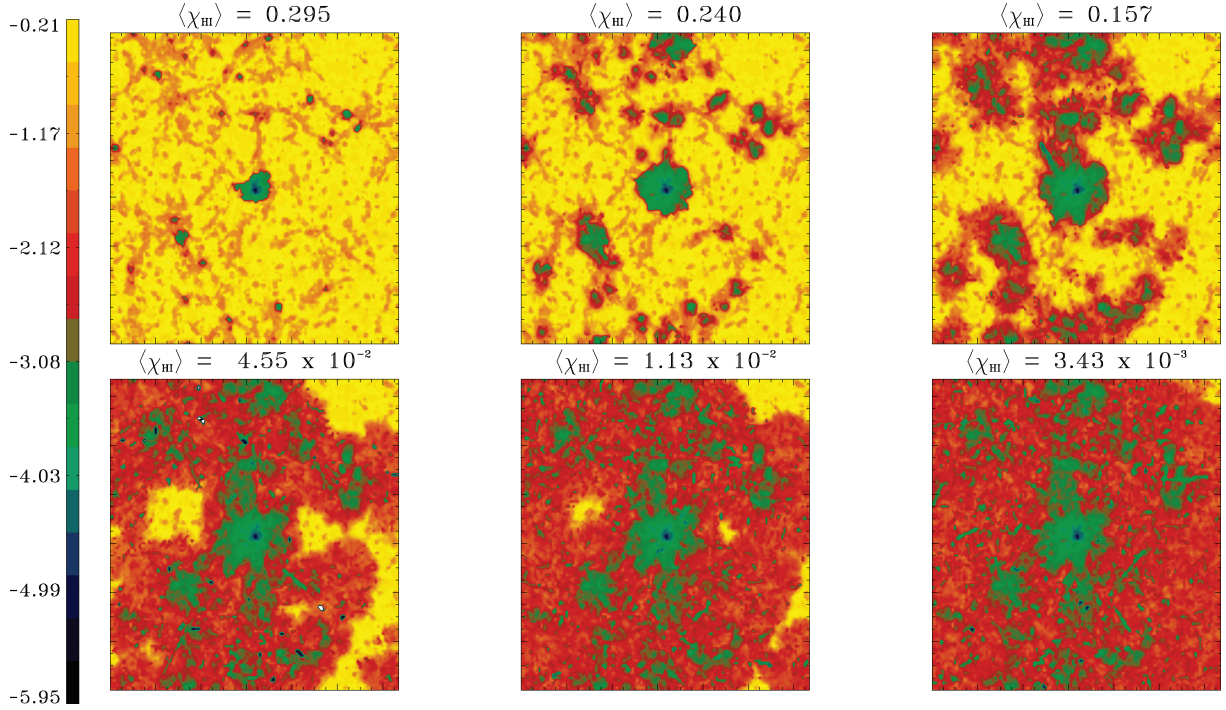
Figure 1. Maps showing the time evolution of the spatial distribution of H I in a 2D plane cut through a 3D box, obtained by running CRASH on a GADGET-2 snapshot (100 h^{-1} Mpc on a side) at $z \sim 6.1$. The colour bar shows the values (in log scale) of the fraction of neutral hydrogen, $\chi_{\rm H I}$. The average decreasing neutral hydrogen fractions marked above each panel, $\langle \chi_{\rm H I} \rangle = 0.295$, 0.24, 0.157, 4.45×10^{-2}, 1.13×10^{-2}, 3.43×10^{-3}, correspond to increasing CRASH runtimes of 10, 50, 100, 200, 300, 500 Myr, respectively. Details are given in Section 2.

formation time 50, 100, 200, 300 Myr, $\langle \chi_{\rm H I} \rangle$ decreases to $\sim$0.24, 0.16, 4.5×10^{-2}, 1.1×10^{-2}, respectively.

Finally at about 300 Myr (lower-centre panel), the simulation volume is almost completely ionized. This configuration corresponds to the post-overlap phase which leads to a further acceleration of the reionization process. For about 400 Myr of star formation activity, $\langle \chi_{\rm H I} \rangle$ drops to a value of about 4.3×10^{-3}. This is a consequence of the fact that, as the IGM becomes more ionized, even the ionizing radiation from the numerous smaller galaxies contributes to the overall radiation field. It is very important to point out that, even in this final stage, the ionization field is highly inhomogeneous, with regions of higher ionization fraction corresponding to the environment of point ionizing sources (green regions in the maps). This topology is of fundamental importance in the estimation of the Lyα LFs, as the Lyα transmissivity associated with each source depends on the extent of the highly ionized regions as well as on the residual neutral hydrogen within them; a very tiny fraction of residual neutral hydrogen is sufficient to suppress the intrinsic Lyα luminosity significantly. Even for an ionization fraction, $\langle \chi_{\rm H I} \rangle \sim 3.4 \times 10^{-3}$, which results after 500 Myr of star formation, the transmission value ranges between 42 and 48 per cent for galaxies with increasing $\dot{M}_*$; the blue part of the line can be significantly attenuated even by the tiny residual fraction of about 10^{-6}, close to the source. As a final note, we again stress that varying $f_{\rm esc}$ would strongly affect both the sizes of the ionized regions and the H I fraction within them, thereby affecting the progression of ionization within the chosen box.

We then post-process each of the CRASH snapshots shown in Fig. 1 and explained above, separately with the Lyα, dust and transmission models which are explained in Sections 3.1, 3.2 and 3.3.

It is important to mention that a single GADGET-2 snapshot suffices for our work because: (i) the Lyα line is a single, narrow line,

which redshifts out of resonance with H I extremely quickly; to a first approximation, the spatial scale imposed by the Gunn–Peterson damping wing on the size of the H II region corresponds to a redshift separation of $\Delta z \approx 4.4 \times 10^{-3}$, i.e. about 280 kpc (physical) at $z = 6$ (Miralda-Escudé 1998), and (ii) the decreasing values of both the density of hydrogen and $\chi_{\rm H I}$ with decreasing redshift render the Lyα line transparent to H I attenuation.

3 THE LAE MODEL

As mentioned in Section 2, for each galaxy in the SPH simulation snapshot, we obtain the SFR, $\dot{M}_*$, the mass-weighted stellar metallicity, Z_*, the total gas mass, $M_{\rm g}$, and the stellar mass, M_*; the stellar age is then calculated as $t_* = M_*/\dot{M}_*$, i.e. assuming a constant SFR. This assumption has been made for consistency with the RT calculation (see Section 2). These properties are then used to calculate the intrinsic Lyα ($L_\alpha^{\rm int}$ [erg s^{-1}]) and continuum luminosity ($L_{\rm c}^{\rm int}$ [erg s^{-1} Å^{-1}]), considering the contribution from both stellar sources and from the cooling of collisionally excited H I in the ISM of the galaxy. The intrinsic values of the Lyα and continuum luminosities so obtained can then be used to calculate the observed luminosity values. It is comparatively easy to calculate the observed continuum luminosity, $L_{\rm c}$, since the wavelength range (1250–1500 Å) of the continuum luminosity band is chosen so as to be unaffected by H I; $L_{\rm c}$ in fact only depends on the fraction of the continuum photons, $f_{\rm c}$, that escape the galactic environment undamped by dust, i.e.

$$L_{\rm c} = L_{\rm c}^{\rm int} f_{\rm c}. \tag{1}$$

On the other hand, since Lyα photons have a large absorption cross-section against H I, the observed Lyα luminosity, L_α, depends both on (i) the fraction of Lyα photons, f_α, that escape out of the

galaxy into the IGM, undamped by dust and (ii) the fraction, T_α, of these 'escaped' photons that are transmitted through the IGM, undamped by H I. The observed Lyα luminosity can therefore be expressed as

$$L_\alpha = L_\alpha^{\text{int}} f_\alpha T_\alpha. \qquad (2)$$

All galaxies with $L_\alpha \geq 10^{42.2}$ erg s^{-1} and an observed equivalent width, EW $= (L_\alpha/L_c) \geq 20$ Å, are identified as LAEs and used to construct the cumulative Lyα and UV LFs which can then be compared to the observations. In principle, our results can be compared to both the observed LFs at $z \sim 5.7$ and 6.6. However, there exists a huge uncertainty between the complete photometric and confirmed spectroscopic sample at $z \sim 6.6$; we limit the comparison between the theoretical model and observations to the data accumulated at $z \sim 5.7$ by Shimasaku et al. (2006), in this work. The calculations of L_α^{int}, L_c^{int}, f_α, f_c and T_α are explained in more detail in what follows.

3.1 The intrinsic luminosity model

Star formation produces photons with energies >1 Ryd, which ionize the H I in the ISM. Due to the high density of the ISM, recombinations take place on a short time-scale and this produces a large number of Lyα photons. The stellar luminosity component is calculated by using STARBURST99 (Leitherer et al. 1999), a population synthesis code, to obtain the spectra and, hence, the H I ionizing photon rate (Q) of each galaxy, using a Salpeter IMF, Z_*, t_* and $\dot{M}_*$ as input parameters. Then the intrinsic Lyα luminosity produced by stellar sources L_α^*, is calculated as

$$L_\alpha^* = \frac{2}{3}(1 - f_{\text{esc}})Qh\nu_\alpha, \qquad (3)$$

where $f_{\text{esc}} = 0.02$ for consistency with the RT calculation (see Section 2), h is the Planck constant, ν_α is the frequency of the Lyα photons and the factor of two-thirds enters assuming case B recombination (Osterbrock 1989). The intrinsic continuum luminosity produced by stellar sources, L_c^*, is calculated at 1375 Å, at the middle of the continuum band between 1250 and 1500 Å.

The Lyα and continuum luminosity from the cooling of collisionally excited H I in each galaxy (L_α^g, L_c^g, respectively) is calculated using the number density of electrons and H I, which depend on the temperature distribution of the ISM gas mass and the gas distribution scale of the galaxy. The temperature dependence comes from the fact that the recombination coefficient, which determines the neutral hydrogen fraction in the ISM, decreases sensitively with higher temperatures. The H I number density is calculated by assuming a primordial ISM composition (76 per cent hydrogen and 24 per cent helium) and calculating the gas distribution scale assuming the H I to be concentrated in a radius, $r_g = 4.5\lambda r_{200}$ (Ferrara, Pettini & Shchekinov 2000), where the spin parameter, $\lambda = 0.04$ and r_{200}, is the virial radius, assuming the collapsed region has an overdensity of 200 times the critical density at the redshift considered. The gas radius is calculated by assuming that the baryons collapse into a centrifugally supported disc in a rotating dark matter halo, such that the angular momentum of the baryonic disc is the same as that of the rotating halo. Complete details of this calculation can be found in Ferrara et al. (2000). The calculation of the electron number density requires the knowledge of the temperature distribution of the IGM gas. However, since we do not have this information from the SPH simulation used in this work, we use the temperature distribution averaged over distinct halo mass ranges shown in table 1 of Dayal et al. (2010) and again use the gas distribution scale to calculate the electron number density. Complete details of this calculation can be found in section 3.2 of Dayal et al. (2010).

3.2 The dust model

It is important to model the dust in the ISM of galaxies since it absorbs both Lyα and continuum photons, thereby strongly influencing the observed luminosity values. Dust is produced both by supernovae and evolved stars in a galaxy. However, several authors (Todini & Ferarra 2001; Dwek, Galliano & Jones 2007) have shown that the contribution of AGB stars can be neglected for $z \gtrsim 5.7$, since the typical evolutionary time-scale of these stars (≥ 1 Gyr) becomes longer than the age of the Universe above that redshift. We therefore make the hypothesis that the dust seen in LAEs at $z \sim 6.1$ is produced solely by Type II supernovae (SNII). We compute the dust enrichment of each LAE by post-processing the CRASH simulation outputs with the dust model described below.

The SNII rate is estimated to be $\gamma \dot{M}_*$, where $\gamma \sim (54\,M_\odot)^{-1}$ for a Salpeter IMF between the lower and upper mass limits of 1 and 100 $M_\odot$, respectively (Ferrara et al. 2000). We have assumed that the progenitors of SNII have a mass larger than 8 $M_\odot$ and in order to simplify the calculation, we have adopted the instantaneous recycling approximation (IRA), i.e. the lifetime of stars with mass larger than 8 $M_\odot$ is zero.

Using this SNII rate, we can calculate the evolution of the total dust mass, $M_{\text{dust}}(t)$, in the galaxy as

$$\frac{dM_{\text{dust}}(t)}{dt} = y_d\gamma\dot{M}_* - \frac{M_{\text{dust}}(t)}{\tau_{\text{dest}}(t)} - \frac{M_{\text{dust}}(t)}{M_g(t)}\dot{M}_*, \qquad (4)$$

where the first, second and third terms on the RHS represent the rates of dust production, destruction and astration (assimilation of a homogeneous mixture of gas and dust into stars), respectively; the initial dust mass is assumed to be zero. Further, y_d is the dust yield per SNII, τ_{dest} is the time-scale of dust destruction due to SNII blast waves and $M_g(t)$ is the gas mass in the galaxy at time t. For y_d, the average dust mass produced per SNII, we adopt a value of 0.54 $M_\odot$ (Todini & Ferarra 2001; Nozawa et al. 2003; Bianchi & Schneider 2007; Nozawa et al. 2007). The amount of gas left in the galaxy, $M_g(t)$, at any time t is calculated as $dM_g(t)/dt = -\dot{M}_*$ and each galaxy is assumed to have an initial gas mass given by the cosmological baryon to dark matter ratio Ω_b/Ω_m.

The destruction time-scale, $\tau_{\text{dest}}(t)$, is estimated following the results of McKee (1989) and Lisenfeld & Ferrara (1998) as

$$\tau_{\text{dest}}(t) = \frac{M_g(t)}{\gamma\dot{M}_*\epsilon M_s(100\,\text{km s}^{-1})}. \qquad (5)$$

Here, ϵ is the efficiency of dust destruction in an SN-shocked ISM, for which we adopt value ~ 0.12; this is a reasonable estimate compared to the value of 0.1 found by McKee (1989). $M_s(100\,\text{km s}^{-1})$ is the mass accelerated to 100 km s^{-1} by the SN blast wave and has a value of 6.8×10^3 $M_\odot$ (Lisenfeld & Ferrara 1998).

Once the final dust mass, $M_{\text{dust}}(t_*)$, is calculated for each galaxy in the simulation, we can translate this into an optical depth, τ_c, for continuum photons as

$$\tau_c(r_d) = \frac{3\Sigma_d}{4as}, \qquad (6)$$

where $\Sigma_d = M_{\text{dust}}(t_*)r_d^{-2}$ is the dust surface mass density, r_d is the radius of dust distribution, a and s are the radius and material density of graphite/carbonaceous grains, respectively ($a = 0.05$ μm, $s = 2.25$ g cm^{-3}; Todini & Ferarra 2001; Nozawa et al. 2003). This can be used to obtain the escape fraction of continuum photons from the galaxy as $f_c = e^{-\tau_c}$. The value of r_d is adjusted so as to reproduce the UV LF data in Section 4 and complete details of the calculations mentioned here can be found in Dayal et al. (2010).

Different extinction curves, including that for the Milky Way, Small Magellanic Cloud and supernovae give different relations

between the extinction of the Lyα and continuum photons, for homogeneously distributed dust. In this spirit, and to get a hint of the dust inhomogeneity, we combine f_α and f_c, and use the escape fraction of Lyα photons relative to the continuum ones, f_α/f_c, to be the free parameter to calculate L_α in our model. A more detailed explanation of the determination of f_c and f_α, required to reproduce the observations, follows in Section 4.

3.3 The IGM transmission model

The calculation of T_α is now explained in detail in this section. If z_{em} and z_{obs} are the redshifts of the emitter and the observer, respectively, we calculate the total optical depth (τ_α) to the Lyα photons along a line of sight (LOS) as

$$\tau_\alpha(v) = \int_{z_{em}}^{z_{obs}} \sigma_0 \phi(v) n_{H_I}(z) \frac{dl}{dz} \, dz, \qquad (7)$$

where $v = (\lambda - \lambda_\alpha)[\lambda_\alpha c]^{-1}$ is the rest-frame velocity of a photon with wavelength λ, relative to the line centre (rest-frame wavelength $\lambda_\alpha = 1216$ Å, velocity $v_\alpha = 0$), ϕ is the Voigt profile, n_{H_I} is the number density of H I along the LOS, $dl/dz = c[H(z)(1 + z)]^{-1}$ and c represents the light speed. We use $\sigma_0 = \pi e^2 f[m_e c]^{-1}$, where e, m_e are the electron charge and mass respectively and f is the oscillator strength (0.4162). Then, the transmission for any photon of velocity v can be expressed as $T_\alpha(v) = e^{-\tau_\alpha(v)}$.

For regions of low H I density, the natural line broadening is not very important and the Voigt profile can be approximated by the Gaussian core:

$$\phi(v_i) \equiv \phi_{gauss} = \frac{\lambda_\alpha}{\sqrt{\pi}b} e^{-\left(\frac{v_i + v_p - v_\alpha}{b}\right)^2}, \qquad (8)$$

where v_i is the velocity of a photon of initial velocity v at a redshift z_i along the LOS, v_p is the peculiar velocity at z_i and v_α is the velocity of the Lyα photons at z_i, which is 0 in this expression. The Doppler width parameter is expressed as $b = \sqrt{2kT/m_H}$, where m_H is the hydrogen mass, k is the Boltzmann constant and T is the IGM temperature. While we use a $T = 10^4$ K for each cell with an ionization fraction $(1 - \chi_{H_I}) \geq 0.1$, we use $T = 20$ K if the IGM is pristine, i.e. has an ionization fraction $(1 - \chi_{H_I}) \leq 0.1$.[2]

In more dense regions the Lorentzian damping wing of the Voigt profile becomes important. According to Peebles (1993), this can be approximated as

$$\phi_{lorentz}(v_i) = \frac{R_\alpha \lambda_\alpha}{\pi \left[(v_i + v_p - v_\alpha)^2 + R_\alpha^2\right]} \qquad (9)$$

where $R_\alpha = \Lambda \lambda_\alpha [4\pi]^{-1}$ and $\Lambda = 6.25 \times 10^8 \, s^{-1}$ is the decay constant for the Lyα resonance. Although computationally more expensive than the above approximations, using the Voigt profile to compute the absorption cross-section gives precise results, and therefore we have implemented it in our code to obtain all the results presented below.

We briefly digress here to discuss the effects of the peculiar velocities, v_p (equations 8 and 9) on $T_\alpha(v)$. If v_p is negative (positive) with respect to the velocity, v, of an emitted Lyα photon, i.e. there is an inflow towards (outflow from) the galaxy, $v_i + v_p \propto (\lambda_i - \lambda_\alpha)$ decreases (increases). Therefore, λ_i is smaller (larger) than it would be in the case of $v_p = 0$, i.e. the wavelength has been blueshifted

---

(redshifted). Consequently, the values of the $e^{-v_i + v_p}$ and $1/[v_i + v_p]$ terms (equations 8 and 9) increase (decrease) which leads to a higher (lower) value of $\tau_\alpha(v)$, i.e. a lower (higher) value of $T_\alpha(v)$. In brief, using the above Voigt profile, peculiar velocities caused by galactic scale inflows (outflows) of gas blueshift (redshift) the Lyα photons, leading to a lower (higher) value of T_α.

The total Lyα optical depth is calculated for each galaxy identified in the CRASH outputs corresponding to $\langle \chi_{H_I} \rangle \sim 0.29, 0.24, 0.16, 4.5 \times 10^{-2}, 1.1 \times 10^{-2}, 4.3 \times 10^{-3}, 3.4 \times 10^{-3}$ as mentioned in Section 2. The transmission along any LOS is calculated as $T_\alpha(v) = e^{-\tau_\alpha(v)}$, integrating from the position of each galaxy to the edge of the box. To get a statistical estimate of the transmission, we construct six LOS starting from the position of each galaxy, one along each of the box axes, for each of the mentioned ionization states. The average value of the transmission for each galaxy is then obtained by averaging the transmission over the six LOS. This is done for all the ionization state configurations resulting from the RT calculation.

Once the value of f_{esc} is fixed (to 0.02 in this work), the only *two free parameters* of our model to match the theoretical Lyα and UV LFs to the observed ones are the dust distribution radius, r_d, relative to the gas radius, r_g and the relative escape fraction of Lyα photons as compared to the continuum photons, f_α/f_c. Both these parameters remain quite poorly understood due to a lack of observational data about the dust distribution/topology in high-redshift galaxies; they must therefore be inferred by comparing the theoretical LFs to the observed ones. Details on how these parameters are determined follow in Section 4.

4 LAE VISIBILITY DURING REIONIZATION

Once the combined SPH+RT calculations are carried out and the LAE model implemented, we are in a position to quantify the importance of reionization, peculiar velocities and the dust enrichment on the observed LFs. Physically, the reionization process leads to a decrease in $\langle \chi_{H_I} \rangle$, thereby increasing T_α; on the other hand, peculiar velocities caused by galactic scale outflows (inflows), redshift (blueshift) the Lyα photons, thereby leading to a higher (lower) value of T_α as explained in Section 3.3. A handle on the dust enrichment is necessary since dust grains absorb both Lyα and continuum photons, thereby affecting their escape fractions from the galaxy.

4.1 The LFs for dust-free galaxies and a stationary IGM

We begin our study by ignoring the effects of the peculiar velocities and assuming all the galaxies to be dust free, to quantify how each of these two parameters shape the observed Lyα and UV LFs. The former assumption means that $v_p = 0$ in equations (8) and (9); the latter implies that all photons produced inside the galaxy escape into the IGM, i.e. $f_c = f_\alpha = 1$ in equations (1) and (2). We then use the prescriptions detailed in Section 3 to identify the galaxies that would be visible as LAEs in each CRASH output and build their Lyα LF as shown in Fig. 2.

Since both peculiar velocities and dust are neglected, in this case, while the UV LF is simply the intrinsic LF, the Lyα LF is shaped solely by the transmission through the IGM. As mentioned in Section 2, after a star formation time-scale as short as 10 Myr ($\langle \chi_{H_I} \rangle \sim 0.29$), the galaxies in the simulation snapshot are able to form H II regions, with the region size and the ionization fraction inside it increasing with $\dot{M}_*$; this results in T_α which increases with $\dot{M}_*$. As the galaxies continue to form stars, the sizes of the H II regions built by each source increase with time, leading $\langle \chi_{H_I} \rangle$ to

---

[2] We find that even for an average neutral hydrogen fraction as high as $\langle \chi_{H_I} \rangle \sim 0.295$, only eight cells out of 128^3 have $(1 - \chi_{H_I}) \leq 0.1$, with the complete RT simulation as described in Section 2. Hence, to simplify the calculations, we use $T = 10^4$ K for all the cells for all the CRASH outputs.
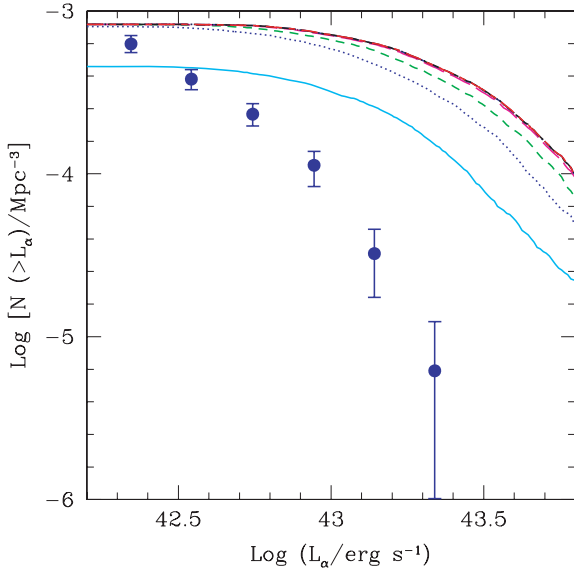
Figure 2. Cumulative Lyα LF for galaxies identified as LAEs from the SPH simulation snapshot including the full RT calculation and density fields but ignoring velocity fields ($v_{\rm p} = 0$) and dust ($f_\alpha = f_{\rm c} = 1$). The lines from bottom to top correspond to CRASH outputs with decreasing values of $\langle \chi_{\rm HI} \rangle$ such that: $\langle \chi_{\rm HI} \rangle \simeq 0.29$ (solid), 0.24 (dotted), 0.16 (short dashed), 4.5×10^{-2} (long dashed), 1.1×10^{-2} (dot–short dashed), 4.3×10^{-3} (dot-long dashed) and 3.4×10^{-3} (short-long dashed). Points show the observed LF at $z \sim 5.7$ (Shimasaku et al. 2006).

decrease to 0.24, 0.16 at $t = 50, 100$ Myr, respectively. This leads to an increase in the transmission of the red part of the Lyα line for all the sources, in turn yielding a corresponding increase of the Lyα luminosity of each source, as depicted in Fig. 2. However, after about 200 Myr, $\langle \chi_{\rm HI} \rangle$ reduces to ~ 0.04; the H II regions built by each source are large enough so that almost all of the red part of the Lyα line is transmitted and the value of T_α saturates for all LAEs. This results in very similar LFs for $\langle \chi_{\rm HI} \rangle \leq 0.04$, as seen from the same figure.

The key point here is that if peculiar velocities and dust effects are neglected, at no point in the reionization history, either the slope or the amplitude of the observed Lyα LF can be reproduced; analogous problems also arise when the UV LFs are considered.

4.2 The LFs for dusty galaxies and a stationary IGM

The above discussion implies the need of one or more physical effects attenuating the Lyα and continuum photons, the most obvious of which is the presence of dust in the ISM of these galaxies, which would absorb both Lyα and continuum photons, simultaneously reducing f_α and $f_{\rm c}$ (models S1–S7, Table 1). We then include the dust model described in Section 3.2 into our calculations. Since the UV is unaffected by the H I in the IGM as mentioned in Section 3, the same value of $r_{\rm d} = 0.48 r_{\rm g}$ ($r_{\rm g}$ is the ISM gas distribution scale; Section 3.2) reproduces the UV LF for all of the ionization states of the IGM, ranging from $\langle \chi_{\rm HI} \rangle \sim 0.29$ to 3.4×10^{-3}. This assumption of the dust distribution scale leads to an average escape fraction of continuum photons, $f_{\rm c} \sim 0.12$ (refer to Section 3.2 for details) for the galaxies we identify as LAEs.

We now momentarily digress to discuss the effect of reionization on T_α (defined by equation 2) for different stellar mass ranges. However, since $\dot{M}_*$ scales with M_* (details in Section 5), we discuss T_α in terms of $\dot{M}_*$. As mentioned in Section 2, we initialize the

CRASH runs with $\langle \chi_{\rm HI} \rangle \sim 0.3$. In a star formation time-scale of 10 Myr (model S1, Table 1), by virtue of the H II regions that already start growing, the total photoionization rate (sum of contributions from the UVB and all the galaxies in the simulation) has a value of $\Gamma_T{}^3 = 2.8 \times 10^{-17}\,{\rm s}^{-1}$ and $\langle \chi_{\rm HI} \rangle$ decreases slightly to 0.295. At this point, due to their smaller H I ionizing photon output, galaxies with $\dot{M}_* \leq 25\,{\rm M_\odot\,yr^{-1}}$ have $T_\alpha \sim 0.2$; galaxies with larger $\dot{M}_*$ have $T_\alpha \sim 0.3$, as shown in Panel (a) of Fig. 3. As the star formation continues, for 50 (100) Myr of star formation (models S2 and S3, respectively, Table 1), the H II region sizes increase and Γ_T increases slightly to $\sim 4.0 \times 10^{-17}$ (7.7×10^{-17}) s^{-1} ; T_α increases and ranges between 0.28 and 0.4 (0.34–0.44) for $\dot{M}_* \sim 8$–200 M$_\odot$ yr^{-1} (see Panels b and c of Fig. 3). Finally for $\Gamma_T \sim 3.3 \times 10^{-16}\,{\rm s}^{-1}$, corresponding to $\langle \chi_{\rm HI} \rangle \sim 0.04$ (model S4, Table 1), the transmission settles to $T_\alpha \sim 0.4$–0.48 for $\dot{M}_* \sim 8$–200 M$_\odot$ yr^{-1} (Figs 3d–f, models S5–S7, Table 1); in about 200 Myr from the ignition of star formation, the Strömgren spheres built by these LAEs are large enough so that the redshifted Lyα photons are no longer affected by the H I outside this region. However, the residual H I inside this ionized region leads to an absorption of the photons bluewards of the Lyα line, and hence, about half of the line is transmitted. The values of Γ_T, $\langle \chi_{\rm HI} \rangle$ and the T_α values averaged for all LAEs in each CRASH output are shown in Table 1.

Using the above T_α values and dust model fixed by the UV LF, the only free parameter we are left with, to match the theoretical and observed Lyα LFs, is $f_\alpha/f_{\rm c}$; this only scales the Lyα LF without affecting its shape. As mentioned above, the T_α value for galaxies identified as LAEs settles for $\langle \chi_{\rm HI} \rangle \leq 0.04$, which leads to a corresponding saturation in the Lyα LF. We find that $f_\alpha/f_{\rm c} \sim 1.3$ reproduces the slope and the magnitude of the observed Lyα LF quite well for all the CRASH outputs where $\langle \chi_{\rm HI} \rangle \leq 0.04$ (models S4–S7, Table 1), as shown in Fig. 4. However, due to decreasing values of T_α, the Lyα LF is progressively underestimated for increasing values of $\langle \chi_{\rm HI} \rangle$, as seen from the same figure.

4.3 The LFs including dust and IGM peculiar velocities

Once the above framework is in place, we include and study the effect of the final component that can affect the observed luminosity, and the presence of peculiar velocities (models M1–M7, Table 1). Once this is done by consistently deriving the peculiar velocity field from the simulations, we again reproduce both the magnitude and slope of the observed UV LF as shown in Fig. 5. Of course, this does not come as a surprise since velocity fields do not affect UV photons. However, as explained in Section 3.3, galactic scale outflows (inflows) from a galaxy, redshift (blueshift) the Lyα photons, thereby leading to a higher (lower) T_α value. It is quite interesting to see that we can again match the theoretical Lyα LFs to the observed ones by a simple scaling between f_α and $f_{\rm c}$ for $\langle \chi_{\rm HI} \rangle \leq 0.04$ (models M4–M7, Table 1), as seen from Fig. 6. However, we require a much higher value of $f_\alpha/f_{\rm c} \sim 3.7$, compared to the value of 1.3 excluding velocity fields (models S4–S7, Table 1). Again, T_α, and

---

[3] Γ_T, the total photoionization rate, is calculated assuming ionization-recombination equilibrium over average values of density and ionization fraction in the simulation volume, so that

$$\Gamma_T = \frac{(1 - \langle \chi_{\rm HI} \rangle)^2 \langle n_{\rm H} \rangle \alpha_{\rm B}}{\langle \chi_{\rm HI} \rangle}.$$

Here, $\langle n_{\rm H} \rangle$ is the average hydrogen number density in the simulation volume and $\alpha_{\rm B}$ is the case B recombination coefficient.

Table 1. The model designation (Col 1), the star formation time-scale to ionize the IGM (Col 2), the features included in the model (VF stands for peculiar velocity fields) (Col 3), the average neutral hydrogen fraction (Col 4), the value of the total photoionization rate (sum of the contribution from the UVB and from all the galaxies in the snapshot) corresponding to this neutral hydrogen fraction (Col 5), the average transmission for all the galaxies identified as LAEs (Col 6), the average escape fraction of continuum photons for LAEs for the model presented in Section 3.2 (Col 7), the average colour excess value corresponding to this continuum escape fraction using the supernova extinction curve (Col 8) and the relative escape fraction of Lyα and continuum photons to best fit the observations for $\langle \chi_{HI} \rangle \leq 0.04$ (Col 9).

| Model	T (Myr)	Features	$\langle \chi_{HI} \rangle$	Γ_T $(10^{-14}\,\text{s}^{-1})$	$\langle T_\alpha \rangle$	$\langle f_c \rangle$	$\langle E(B-V) \rangle$	f_α / f_c
S1	10	RT + dust	0.295	2.8×10^{-3}	0.21	0.12	0.2	1.3
S2	50	RT + dust	0.240	4.0×10^{-3}	0.30	0.12	0.2	1.3
S3	100	RT + dust	0.157	7.6×10^{-3}	0.37	0.12	0.2	1.3
S4	200	RT + dust	4.55×10^{-2}	3.3×10^{-2}	0.42	0.12	0.2	1.3
S5	300	RT + dust	1.13×10^{-2}	0.14	0.43	0.12	0.2	1.3
S6	400	RT + dust	4.33×10^{-3}	0.33	0.44	0.12	0.2	1.3
S7	500	RT + dust	3.43×10^{-3}	0.48	0.44	0.12	0.2	1.3
M1	10	RT + VF + dust	0.295	2.8×10^{-3}	0.10	0.12	0.2	3.7
M2	50	RT + VF + dust	0.240	4.0×10^{-3}	0.13	0.12	0.2	3.7
M3	100	RT + VF + dust	0.157	7.6×10^{-3}	0.15	0.12	0.2	3.7
M4	200	RT + VF + dust	4.55×10^{-2}	3.3×10^{-2}	0.16	0.12	0.2	3.7
M5	300	RT + VF + dust	1.13×10^{-2}	0.14	0.17	0.12	0.2	3.7
M6	400	RT + VF + dust	4.33×10^{-3}	0.33	0.17	0.12	0.2	3.7
M7	500	RT + VF + dust	3.43×10^{-3}	0.48	0.17	0.12	0.2	3.7
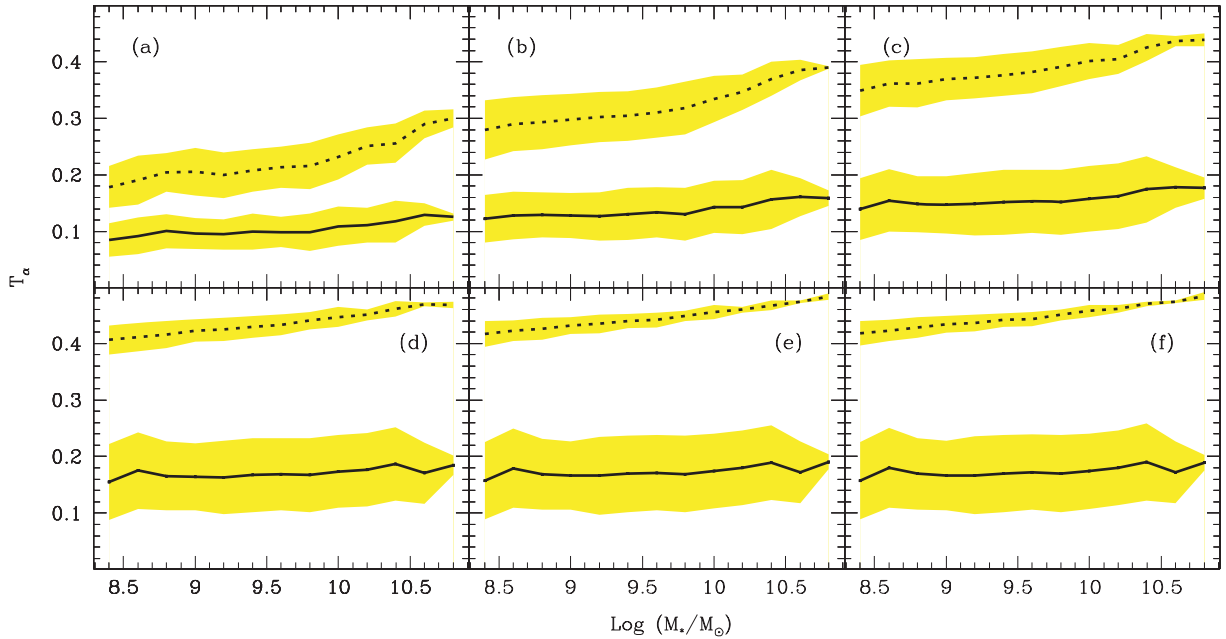
Figure 3. T_α as a function of M_* for galaxies identified as LAEs from the simulation snapshot including the full RT calculation, density fields, dust and ignoring (including) velocity fields shown by dotted (solid) lines in each panel. The solid/dotted lines in each panel correspond to the following models given in Table 1: (a) M1/S1 ($\langle \chi_{HI} \rangle \sim 0.29$), (b) M2/S2 (0.24), (c) M3/S3 (0.16), (d) M4/S4 (4.5×10^{-2}), (e) M5/S5 (1.1×10^{-2}) and (f) M7/S7 (3.4×10^{-3}). In each panel, the stellar mass bins span 0.2 dex and the shaded regions represent the 1σ error bars in each mass bin.

hence the Lyα LF, get progressively more damped with an increase in $\langle \chi_{HI} \rangle$, as seen from Fig. 6 (models M3–M1, Table 1).

We now discuss the reason for the higher $f_\alpha/f_c \sim 3.7$ value required to reproduce the Lyα LF when velocity fields are considered, as compared to the ratio of 1.3, when they are not, for $\langle \chi_{HI} \rangle \leq 0.04$. The galaxies we identify as LAEs have halo masses $M_h \sim 10^{10.4-12}\,\text{M}_\odot$, which correspond to $\geq 2\sigma$ fluctuations at $z \sim 6.1$. These LAEs are therefore subject to strong inflows since they lie in dense regions. As these inflows blueshift the Lyα photons, even photons in the red part of the line are attenuated, thereby reducing T_α. This can be seen clearly from Fig. 3, where the solid lines, which represent the outcomes from the models including velocities, are always significantly below the dotted ones, which represent the model with no velocity field included. When velocity fields are included we find $T_\alpha \sim 0.08$–0.12 (0.16–0.18) for $\langle \chi_{HI} \rangle \sim$ 0.29 (3.4×10^{-3}) for $\dot{M}_* \sim 8$–$200\,\text{M}_\odot\,\text{yr}^{-1}$. Averaging over all the LAEs for $\langle \chi_{HI} \rangle \sim 3.4 \times 10^{-3}$, we find the value of $T_\alpha \sim 0.17$ (0.44) including (excluding) the effects of peculiar velocity fields. This requires that when peculiar velocities are included, a correspondingly larger fraction (0.44/0.17 = 2.6) of Lyα photons must escape the galaxy, undamped by dust to bring the observed luminosity up to the levels it would reach in the absence of these inflows. Although
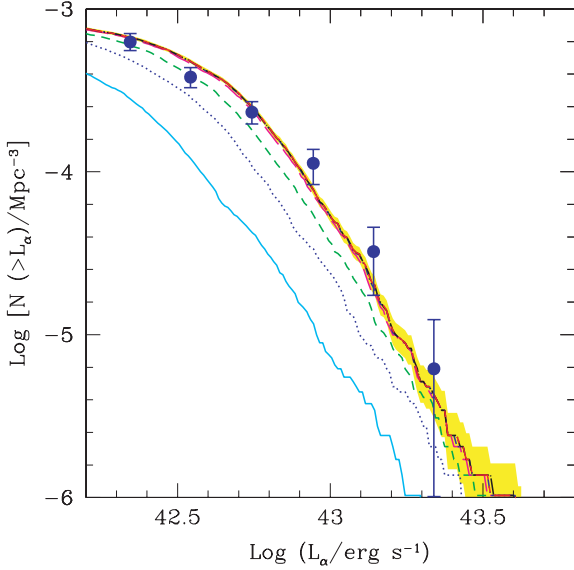
Figure 4. Cumulative Lyα LF for galaxies identified as LAEs from the SPH simulation snapshot including the full RT calculation, density fields and dust but ignoring velocity fields ($v_p = 0$), corresponding to models S1–S7 in Table 1. The lines from bottom to top correspond to CRASH outputs with decreasing values of $\langle\chi_{HI}\rangle$ such that $\langle\chi_{HI}\rangle \sim 0.29$ (solid), 0.24 (dotted), 0.16 (short dashed), 4.5×10^{-2} (long dashed), 1.1×10^{-2} (dot-short dashed), 4.3×10^{-3} (dot-long dashed) and 3.4×10^{-3} (short-long dashed). The shaded region shows the Poissonian error corresponding to $\langle\chi_{HI}\rangle \sim 3.4 \times 10^{-3}$, i.e. model S7 (Table 1) and points show the observed LF at $z \sim 5.7$ (Shimasaku et al. 2006).
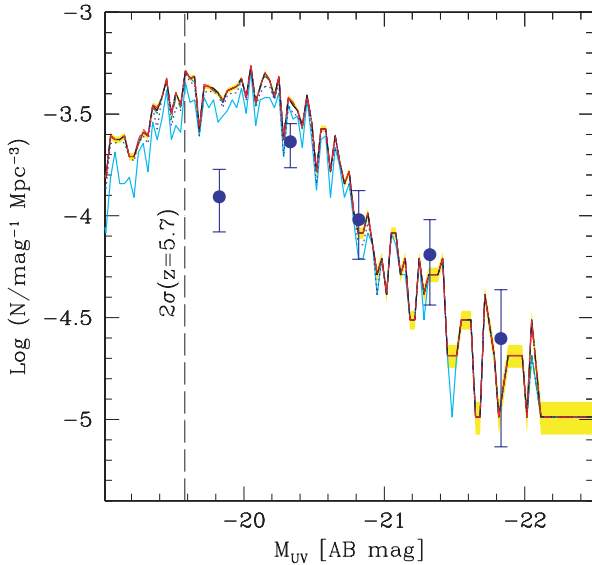

Figure 5. UV LF for galaxies identified as LAEs from the simulation snapshot including the full RT calculation, density fields, velocity fields and dust, corresponding to models M1 to M7 in Table 1. The lines from bottom to top correspond to decreasing values of $\langle\chi_{HI}\rangle$ such that: $\langle\chi_{HI}\rangle \sim 0.29$ (solid), 0.24 (dotted), 0.16 (short dashed), 4.5×10^{-2} (long dashed), 1.1×10^{-2} (dot-short dashed), 4.3×10^{-3} (dot-long dashed) and 3.4×10^{-3} (short-long dashed). The shaded region shows the Poissonian error corresponding to $\langle\chi_{HI}\rangle \sim 3.4 \times 10^{-3}$, i.e. model M7 (Table 1) and points show the observed UV LF at $z \sim 5.7$ (Shimasaku et al. 2006).
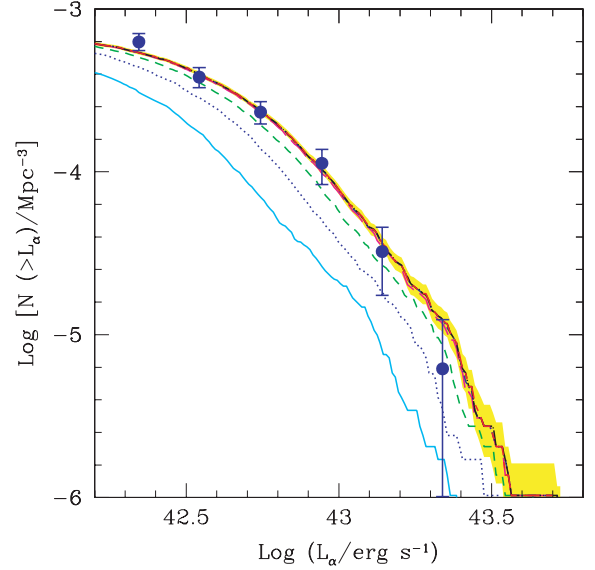

Figure 6. Cumulative Lyα LF for galaxies identified as LAEs from the simulation snapshot including the full RT calculation, density fields, velocity fields and dust, corresponding to models M1 to M7 in Table 1. The lines from bottom to top correspond to decreasing values of $\langle\chi_{HI}\rangle$ such that: $\langle\chi_{HI}\rangle \sim 0.29$ (solid), 0.24 (dotted), 0.16 (short dashed), 4.5×10^{-2} (long dashed), 1.1×10^{-2} (dot-short dashed), 4.3×10^{-3} (dot-long dashed) and 3.4×10^{-3} (short-long dashed). The shaded region shows the Poissonian error corresponding to $\langle\chi_{HI}\rangle \sim 3.4 \times 10^{-3}$, i.e. model M7 (Table 1) and points show the observed LF at $z \sim 5.7$ (Shimasaku et al. 2006).

many galaxies do show outflows, powered by supernova explosions, these dominate at very small scales (≤ 170 physical Mpc). However, the small redshift boost imparted by these is negligible compared to the blueshifting of the Lyα line because of large-scale inflows; eventually, it is these dominant inflows that determine the value of T_α.

Further, including velocity fields changes the slope of the LF; when velocity fields are not included, T_α basically scales with $\dot{M}_*$; when these are included, T_α is the most damped for the largest masses, since these see the strongest inflow velocities by virtue of their largest potential wells. This can be seen clearly from Fig. 3 where the slope of T_α is visibly shallower for the solid curves (including velocities) than for the dotted ones (neglecting velocities). This has the effect of *flattening* the slope of the Lyα LF as can be seen in Fig. 6.

4.4 The $f_\alpha - T_\alpha$ degeneracy and the dusty nature of LAEs

As an important result, the above analysis shows that there exists a degeneracy between the ionization state of the IGM and dust clumping (or grain properties) inside high-redshift galaxies, i.e. a high (low) T_α can be compensated by a low (high) f_α. This is shown in Fig. 7, where we find that within a 1σ error, for $f_\alpha/f_c \sim$ 3.4–4.1, we cannot distinguish an IGM with $\langle\chi_{HI}\rangle \sim 3.4 \times 10^{-3}$ from one where $\langle\chi_{HI}\rangle \sim 0.16$. Within the area under the 5σ error, $f_\alpha/f_c \sim$ 4.1–5.7 can also fit the Lyα LF for $\langle\chi_{HI}\rangle \sim 0.24$. This leads to the very interesting conclusion that the ionization state of the IGM cannot be tightly constrained unless the relative escape fraction of Lyα compared to the continuum photons is reasonably well understood.

We now discuss the dusty nature of the LAEs we identify from the SPH simulation. We require that for the complete LAE model
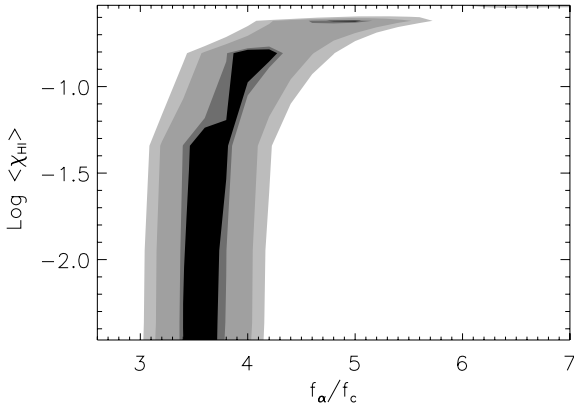
Figure 7. The $1 - 5\sigma$ probability contours (black to light grey, respectively) for combinations of $\langle\chi_{H_I}\rangle$ and f_α/f_c that fit the observed Lyα LF. Within a 1σ (5σ) error, we cannot distinguish an IGM with $\langle\chi_{H_I}\rangle \sim 3.4 \times 10^{-3}$ from one where $\langle\chi_{H_I}\rangle \sim 0.16$ (0.24) for $f_\alpha/f_c \sim 3.4$–4.1 (3.0–5.7). This implies a *degeneracy* between the ionization state of the IGM and dust clumping (or grain properties) inside high-redshift galaxies; the ionization state of the IGM cannot be tightly constrained unless the relative escape fraction of Lyα compared to the continuum photons is reasonably well understood. Refer to Section 4 for details.

(M1–M7, Table 1), the value of f_α/f_c must range between 3.4 and 4.1 (3 and 5.7) for an average neutral hydrogen fraction of $\langle\chi_{H_I}\rangle \leq 0.16$ ($\leq$0.24). However, no single extinction curve gives a value of $f_\alpha/f_c > 1$. One of the simplest ways of explaining this large relative escape fraction is to invoke the multiphase ISM model as proposed by Neufeld (1991), wherein the ISM is multiphase and consists of a warm gas with cold dust clumps embedded in it. This inhomogeneity of the dust distribution can then lead to a larger attenuation of the continuum photons relative to the Lyα.

We also translate f_c into the colour excess, $E(B - V)$, for models M1–M7 (Table 1) and compare this value to other high-redshift LAE observations. At high redshifts, the observed properties of the most distant quasars (Maiolino et al. 2006) and gamma-ray bursts (Stratta et al. 2007) can be successfully interpreted using an SN extinction curve (Todini & Ferrara 2001; Bianchi & Schneider 2007). Using the same curve, we find the average value of the colour excess, $E(B - V) = 0.2$, corresponding to an average $f_c = 0.12$. When expressed in terms of the widely used Calzetti extinction law (Calzetti et al. 2000), the average value of $f_c = 0.12$ corresponds to a colour excess $E(B - V) = 0.21$. This average inferred colour excess value is in very good agreement with recent experimental determinations: by fitting the SEDs of three LAEs at $z = 5.7$, Lai et al. (2007) have inferred $E(B - V) < 0.225$–0.425; in a sample of 12 LAEs at $z = 4.5$, Finkelstein et al. (2009) have found $E(B - V) = 0.04$–0.37 and by fitting the SEDs of nine LAEs at $z \sim 5$, Pirzkal et al. (2007) have inferred $E(B - V) = 0.01$–0.15. Further, using SPH simulations similar to those used here, Nagamine et al. (2008) have inferred a value of $E(B - V) \sim 0.15$; this difference can be attributed to the fact that these authors use a single value of the IGM transmission across all galaxies. However, a number of other authors have inferred extremely low values of the colour excess for LAEs: stacking the SEDs of 23 LAEs at $z \sim 3.1$, Gawiser et al. (2006) have inferred $E(B - V) = 0.02$; stacking the SEDs of 76 LAEs at $z \sim 3.1$, Lai et al. (2008) have calculated $E(B - V) \sim 0$ and, recently, stacking 165 (91) LAEs at $z \sim 5.7$ (6.6), Ono et al. (2010) have inferred $E(B - V) \sim 0$. However, it must be stressed that the colour excess inferred from the observed spectra is degenerate with the stellar mass and the stellar ages; it is possible to reproduce the

same observed spectra by widely different combinations of these parameters, a point also made by Lai et al. (2007) and Dayal et al. (2009).[4]

We now summarize our two main results: (i) we find that the Lyα LF can be well reproduced (to within a 5σ error) by an average neutral hydrogen fraction as high as 0.24 (an almost neutral IGM), to a value as low as 3.4×10^{-3}, corresponding to an ionized IGM, provided that the increase in the transmission is compensated by a decrease in the Lyα escape fraction from the galaxy; (ii) we find that to reproduce the Lyα LF, for any ionization state of the IGM, we require $f_\alpha/f_c > 1$, a value that cannot be obtained using any existing extinction curve; this raises the need to invoke a multiphase ISM model, in which dust clumps are embedded in a highly ionized ISM, to facilitate the Lyα photon escape relative to that of continuum photons.

5 PHYSICAL PROPERTIES OF LAEs

We are now in a position to discuss the physical properties of the galaxies we identify as LAEs, including the stellar and gas mass, metallicity, stellar ages, dust mass and escape fraction of Lyα photons from the ISM. As mentioned in Section 4, while the UV LF is independent of the ionization state of the IGM, the Lyα LF can be well reproduced if a low (high) Lyα escape fraction from the galaxy is compensated by a high (low) transmission through the IGM. Hence, by scaling up f_α/f_c for increasing values of $\langle\chi_{H_I}\rangle > 0.04$ (models M1–M3, Table 1), we would broadly always identify the same galaxy population as LAEs. We now show the physical properties for the LAEs identified using model M7 (Table 1), which includes the full RT calculation, density/velocity fields and dust, with $f_\alpha/f_c = 3.7$.

We find that there is a direct correlation between M_g and M_*; LAEs with a larger M_* are also more gas rich. However, the ratio M_g/M_* is the largest (smallest) for LAEs with the smallest (largest) M_*, as one can deduce from panel (a) of Fig. 8. If we assume the halo mass to scale with the total baryonic mass ($M_g + M_*$), according to the cosmological ratio, this implies that more massive galaxies are more efficient in turning their gas into stars. This trend is as expected, since even a small amount of star formation activity in low-mass galaxies can lead to large outflows of gas, thereby suppressing further star formation. This situation, however, does not occur in galaxies with larger masses, which do not witness large, galactic scale outflows, by virtue of their much larger potential wells (Mac Low & Ferrara 1999).

LAEs with $M_* \leq 10^{9.7}\,M_\odot$ have $\dot{M}_* \sim 8$–25 $M_\odot\,yr^{-1}$, i.e. most of the LAEs have a sustained but not exceptionally large star formation activity. However, galaxies with larger stellar masses are much more efficient in converting their gas into stars, leading to SFR as large as 200 $M_\odot\,yr^{-1}$, as seen from panel (b) of Fig. 8, which is just a positive feedback of the M_g–M_* relation mentioned above.

Although the average age of the galaxies is calculated as $t_* = M_*/\dot{M}_*$, it is interesting to see that all the galaxies we identify as LAEs have $t_* \geq 10$ Myr, as shown in panel (c) of Fig. 8; further the

---

[4] Since the supernova and Calzetti extinction curves yield similar values of $E(B - V)$, refer to fig. 4 of Dayal et al. (2010) for a flavour of f_α [=1.5 (0.6)f_c, shown with open circles and triangles, respectively] as a function of $E(B - V)$ (obtained using the supernova extinction curve), compared to the GALEX LAE sample (Deharveng et al. 2008), *IUE* local starburst sample (McQuade, Calzetti & Kinney 1995; Storchi-Bergmann, Kinney & Challis 1995) and the Atek et al. (2008) sample.
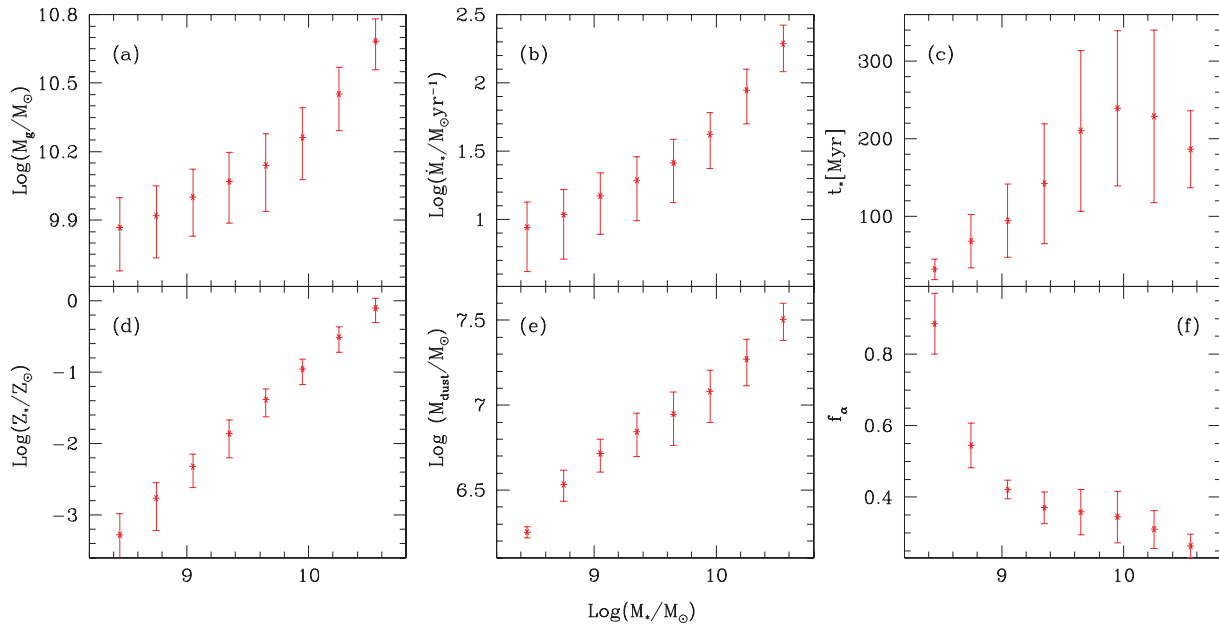
Figure 8. Physical properties of the galaxies identified as LAEs using model M7 in Table 1. This model includes the full RT calculation, density, velocity fields, dust and has $\langle \chi_{HI} \rangle \sim 3.4 \times 10^{-3}$. The panels show (a) the gas mass, M_g, (b) SFR, $\dot{M}_*$, (c) mass-weighted stellar age, t_*, (d) the mass-weighted stellar metallicity, Z_*, (e) the total dust mass, M_{dust}, and (f) the escape fraction of Lyα photons, f_α, plotted as a function of the stellar mass, M_*. The values of each quantity are shown averaged over M_* bins spanning 0.2 dex, with the error bars representing the 1σ error in each bin.

standard deviation on the smallest ages is the smallest. Under the assumption of a constant star formation history, for a given stellar mass, a LAE would be older (younger) if $\dot{M}_*$ in the past was smaller (larger) than the final value at $z \sim 6.1$. It is important to see that the age distribution is in good agreement with that obtained in Dayal et al. (2009) (Panel a1, fig. 3), based on an accurate modelling of the star formation history. However, we are unable to comment on this further in the absence of the complete star formation history for each galaxy. Using these average ages, we find that LAEs are intermediate-age galaxies, instead of being extremely young (<10 Myr) or extremely old (∼1 Gyr) objects. This confirms an earlier result obtained in Dayal et al. (2009) that it is unlikely that young ages could be responsible for the large equivalent widths (EW ≥ 200 Å) observed for a number of LAEs at $z \sim 4.5$, 5.7 by Dawson et al. (2007) and Shimasaku et al. (2006), respectively. A complete discussion on the EW distribution is deferred to Section 6.

The mass-weighted stellar metallicity of LAEs scales with M_* as shown in panel (d) of Fig. 8; LAEs with a higher $\dot{M}_*$ are more dust enriched, which is only to be expected since the metals have a stellar origin. The metallicity values for the smallest haloes show the largest dispersion, possibly arising due to the differing values of feedback in these low-mass haloes. Compared to the analogous mass–metallicity relation observed at lower redshifts (Tremonti et al. 2004; Panter et al. 2008; Maiolino et al. 2008), we do not see the sign of a flattening of metallicity towards larger masses which might imply that at high redshift galaxies are not massive enough to retain their metals and behave as close-boxes.

In our model, we have assumed SNII to be the primary dust factories, with the SNII rate[5] being proportional to $\dot{M}_*$. In our

model, the dust amount is regulated solely by stellar processes: dust is produced by SNII, destroyed in the ISM shocked by SNII and astrated into stars, as mentioned before in Section 3.2. The dust amount, therefore, scales with $\dot{M}_*$, with the most star-forming galaxies being most dust enriched, as shown in panel (e) of Fig. 8. A caveat that must be mentioned here is that as outflows tend to occur on smaller scales with respect to inflows, they are only marginally resolved by our RT simulations. Lacking this information, we have not included their destructive impact into the computation of the dust mass, which could therefore be somewhat overestimated (refer to Dayal et al. 2010 for details).

As expected, we find that f_α decreases with increasing dust enrichment of the galaxy; galaxies with larger M_* and hence $\dot{M}_*$ have a smaller Lyα escape fraction. The value of f_α decreases by a factor of about 3, going from 0.9 to 0.3 as M_* runs from $10^{8.5-10.7}$ M$_\odot$, as shown in panel (f) of Fig. 8.

6 CONCLUSIONS AND DISCUSSION

Although a number of simulations have been used in the past few years (McQuinn et al. 2007; Iliev et al. 2008; Nagamine et al. 2008; Dayal et al. 2009, 2010; Zheng et al. 2010), the relative importance of reionization, velocity fields and dust, on shaping the observed Lyα and UV LFs, has remained rather obscure so far. To this end, we build a coherent model for LAEs, which includes: (i) cosmological SPH simulations run using GADGET-2, to obtain the galaxy properties ($\dot{M}_*$, Z_*, M_*), (ii) the Lyα and continuum luminosities produced, calculated using the intrinsic properties of each galaxy, accounting for both the contribution from stellar sources and cooling of collisionally excited H I in their ISM, (iii) a model for the dust enrichment, influencing the escape fraction of Lyα and continuum photons, and (iv) a complete RT calculation, carried out using CRASH, including the effects of density and velocity fields, used to calculate the transmission of Lyα photons through the IGM.

---

[5] The SNII rate is estimated to be $\gamma \dot{M}_*$, where $\gamma \sim (54 \, M_\odot)^{-1}$ for a Salpeter IMF between the lower and upper mass limits of 1 and 100 M$_\odot$, respectively (Ferrara et al. 2000).

In spite of this wealth of physical effects, we are still left with three free parameters: (i) the value of f_{esc} chosen, which largely affects the ionization field, and hence, T_α, (ii) the radius of dust distribution, r_d, relative to the gas distribution radius, r_g, which determines the optical depth to continuum photons (see equation 6) and (iii) the escape fraction of Lyα photons relative to the continuum photons, f_α/f_c. While the latter two parameters can be constrained by comparing the theoretical model to observations, the value of f_{esc} still remains highly debated. Although we assume a fiducial value of $f_{esc} = 0.02$ (Gnedin et al. 2008) for this work, a different value would affect the intrinsic Lyα luminosity, the sizes of the H II regions built and the χ_{HI} value within these regions. But this problem is alleviated to a large extent because of the $f_\alpha - T_\alpha$ degeneracy shown in Section 4.4; a higher (lower) constant f_{esc} value across all galaxies would, (i) scale the intrinsic Lyα LF down (up) by a constant value and (ii) in general lead to a larger (smaller) T_α. However, these effects could be compensated by varying f_α/f_c appropriately.

Starting our analysis by assuming all galaxies to be dust-free and ignoring gas peculiar velocities, we find that with such a scheme, none of the ionization states of the IGM with $\langle \chi_{HI} \rangle \sim 0.29$ to 3.4×10^{-3} can reproduce either the slope or the galaxy number density of the observed UV or Lyα LF. We then include the dust model described in Section 3.2 into our calculations, such that each SNII produces $0.54 \, M_\odot$ of dust, SNII shocks destroy dust with an efficiency of about 12 per cent and the dust distribution radius is about half of the gas distribution radius, $r_d = 0.48 r_g$. Since the UV is unaffected by the H I in the IGM as mentioned in Section 3, the same dust model parameters reproduce the UV LF for all of the ionization states of the IGM, ranging from $\langle \chi_{HI} \rangle \sim 0.29$ to 3.4×10^{-3}.

We find that we can reproduce the Lyα LF using $f_\alpha/f_c \sim 1.3$ (3.7) for all ionization states such that $\langle \chi_{HI} \rangle \leq 0.04$ excluding (including) peculiar velocity fields, since the Lyα LF settles to a constant value at this point due to a saturation in T_α, as explained in Section 4. Higher values of $\langle \chi_{HI} \rangle$ naturally lead to a lower transmission, thus leading to a progressive underestimation of the Lyα LF. The higher f_α/f_c value required to reproduce the observations when velocity fields are included arise because LAEs reside in $\geq 2\,\sigma$ fluctuations; LAEs are therefore subject to strong inflows which blueshift the Lyα photons, thereby reducing T_α. This decrease in T_α must therefore be compensated by a larger escape fraction from the galaxy to fit the observations. Further, due to the larger masses, T_α is most damped for the largest galaxies, when velocity fields are included, which has the effect of *flattening* the slope of the Lyα LF.

The above *degeneracy* between the ionization state of the IGM and the dust distribution/clumping inside high-redshift galaxies has been quantified (see Fig. 7); the Lyα LF can be well reproduced (to within a 5σ error) by $\langle \chi_{HI} \rangle \sim 0.24$, corresponding to a highly neutral IGM, to a value as low as 3.4×10^{-3}, corresponding to an ionized IGM, provided that the increase in T_α is compensated by a decrease in the Lyα escape fraction from the galaxy. This leads to the very interesting conclusion that the ionization state of the IGM cannot be constrained unless the escape fraction of Lyα versus continuum photons is reasonably well understood. This is possible only through simulations that model the physics of the ISM, including the clumping of dust, and include an RT calculation for both Lyα and continuum photons on such ISM topologies. However, the clumping of dust depends on the turbulence in the ISM, which itself remains only poorly understood. Therefore, attempts to break the mentioned degeneracy must be deferred to future works.

As for the dusty nature of LAEs, we find that $\langle f_c \rangle \sim 0.12$, averaged over all the LAEs in any snapshot, which corresponds to a

colour excess, $E(B - V) \sim 0.21$ (0.2), using a Calzetti (SN) extinction curve. This value is in very good accordance with the observed values obtained using the Calzetti extinction law of $E(B - V) < 0.225$–0.425 (Lai et al. 2007) and $E(B - V) = 0.04$–0.37 (Finkelstein et al. 2009). Secondly, since no single extinction curve (Milky Way, Small Magellanic Cloud, supernova) gives a value of $f_\alpha/f_c > 1$, this larger escape fraction of Lyα photons relative to the continuum can be understood as an indication of a multiphase ISM model (Neufeld 1991) where dust clumps are embedded in a more diffuse ionized ISM component.

LAEs with a larger M_* are also more gas rich. However, the ratio M_g/M_* is the largest (smallest) for LAEs with the smallest (largest) stellar mass, which implies that more massive galaxies ($M_* \geq 10^{10} \, M_\odot$) are more efficient in turning their gas into stars ($\dot{M}_* \geq 40 \, M_\odot \, yr^{-1}$), i.e. star formation is suppressed ($\sim$8–$25 \, M_\odot \, yr^{-1}$) in low-mass galaxies ($M_* < 10^{9.7} \, M_\odot$) due to mechanical feedback. All the galaxies we identify as LAEs have $t_* \sim 10$–300 Myr; LAEs are intermediate-age galaxies, instead of being extremely young (<10 Myr) or extremely old ($\sim$1 Gyr) objects, as shown in Dayal et al. (2009). The mass-weighted stellar metallicity of LAEs scales with M_* but the metallicity of the smallest haloes has a large dispersion, possibly arising due to the increasing importance of feedback towards low-mass haloes. Since in our model, we have assumed SNII to be the primary dust factories, the dust amounts are regulated solely by stellar processes. The dust amounts, therefore, scale with $\dot{M}_*$, with the most star-forming galaxies being most dust enriched. As expected, we find that f_α decreases with increasing dust enrichment of the galaxy; galaxies with larger M_*, and hence $\dot{M}_*$, have a smaller Lyα escape fraction. The value of f_α decreases by a factor of about 3, going from 0.9 to 0.3 as M_* increases from $10^{8.5-10.5} \, M_\odot$.

We finally comment on the EW distribution obtained from our model and compare it to the observations (Fig. 9). There is a trend of increasing EW in more luminous objects which cannot be yet solidly identified in the available (and uncertain) observational data. In addition, the observed EWs show a large dispersion, varying
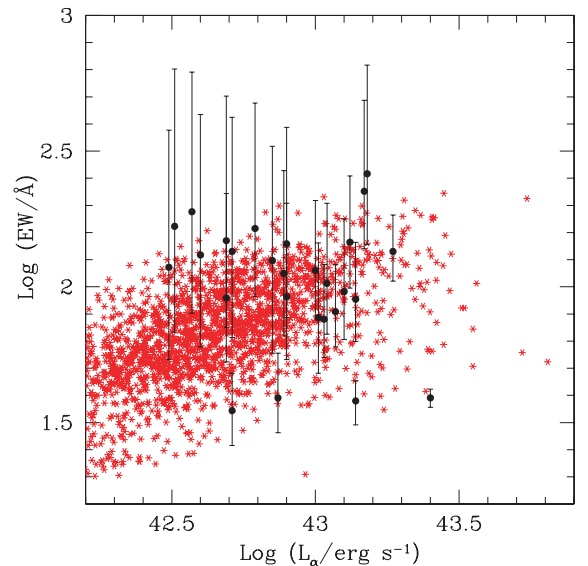

Figure 9. Observed EWs from Shimasaku et al. (2006) (circles) and model values of the observed EWs (asterisks) as a function of the observed Lyα luminosity. The theoretical model includes the full RT calculation, density, velocity fields, dust and has $\langle \chi_{HI} \rangle \sim 3.4 \times 10^{-3}$, corresponding to model M7 (Table 1).

by as much as a factor of 3 for the same L_α value; this suggests that the observed EW depends on several structural parameters of LAEs, namely $\dot{M}_*$, peculiar velocities and dust clumping, to name a few. By virtue of using an LAE model which depends on the intrinsic galaxy properties, includes a dust calculation and takes peculiar velocities/density inhomogeneities into account, we also obtain a large spread (20–222 Å) in the observed EWs. This is a clear improvement on our own previous work (Dayal et al. 2009) in which some of these ingredients were not yet accounted for.

Finally, we discuss a few caveats. First, we have used a constant value of the escape fraction of H I ionizing photons, $f_{esc} = 0.02$, in all our calculations. However, the value of f_{esc} remains poorly constrained both observationally and theoretically. While $z \sim 3$ galaxies have been used to obtain values of $f_{esc} < 0.04$ (Fernandez-Soto, Lanzetta & Chen 2003) to $f_{esc} \sim 0.1$ (Steidel, Pettini & Adelberger 2001), observations in the local Universe range between $f_{esc} < 0.01$ (Deharveng et al. 1997) to $f_{esc} \sim 0.1$–0.73 (Catellanos Díaz & Tenorio-Tagle 2002). A larger (smaller) value of f_{esc} would lead to larger (smaller) H II regions, thereby affecting the progress of the reionization process and hence T_α; a change in f_{esc} would also affect L_α^{int} (Section 3.1). However, this problem is alleviated to a large extent by our result that shows a degeneracy between f_α and T_α; a constant higher (lower) value of f_{esc} would lead to (i) a decrease (increase) in the intrinsic Lyα luminosity, L_α^{int}, and (ii) an increase (decrease) in T_α. However, by scaling f_α/f_c appropriately, we would always be able to reproduce the Lyα LF.

Secondly, the average age of the galaxies is calculated as $t_* = M_*/\dot{M}_*$. Since we calculate the ages assuming constant $\dot{M}_*$, it is entirely possible that some of the LAEs could be slightly older (younger) if $\dot{M}_*$ in the past was smaller (larger) than the final value at $z \sim 6.1$. Galaxies younger than 10 Myr would have higher EWs as compared to the values shown here; however, this could be possible only for the smallest galaxies, which could assemble due to mergers and undergo star formation in a time as short as 10 Myr.

Thirdly, in the dust model explained in Section 3.2, we have considered dust destruction by forward sweeping SNII shocks. However, Bianchi & Schneider (2007) have shown that reverse shocks from the ISM can also lead to dust destruction, with only about 7 per cent of the dust mass surviving the reverse shock, for an ISM density of 10^{-25} gm cm^{-3}. Since we neglect this effect, we might be overpredicting the dust enrichment in LAEs. This, however, does not affect our results because the dust optical depth depends on the surface density of the dust distribution as shown in equation (6); a large (small) dust mass can be distributed in a large (small) volume to obtain identical values of the optical depth.

ACKNOWLEDGMENTS

REFERENCES

Atek H., Kunth D., Hayes M., Ostlin G., Mas-Hesse J. M., 2008, A&A, 488, 491
Bianchi S., Schneider R., 2007, MNRAS, 378, 973
Bouwens R. et al., 2009, ApJ, 705, 936
Calzetti D., Armus L., Bohlin R. C., Kinney A. L., Koornneef J., Storchi-bergmann T., 2000, ApJ, 533, 682
Catellanos M., Díaz Á. I., Tenorio-Tagle G., 2002, ApJ, 565, 79
Dawson S., Rhoads J. E., Malhotra S., Stern D., Wang J., Dey A., Spinrad H., Jannuzi B. T., 2007, ApJ, 671, 1227
Dayal P., Ferrara A., Gallerani S., 2008, MNRAS, 389, 1683
Dayal P., Ferrara A., Saro A., Salvaterra R., Borgani S., Tornatore L., 2009, MNRAS, 400, 2000
Dayal P., Ferrara A., Saro A., 2010, MNRAS, 402, 1449
Deharveng J.-M., Faiesse S., Milliard B., LeBrun V., 1997, A&A, 325, 1259
Deharveng J.-M. et al., 2008, ApJ, 680, 1072
Dijkstra M., Lidz A., Wyithe J. S. B., 2007, MNRAS, 377, 1175
Dwek E., Galliano F., Jones A. P., 2007, Nuovo Cim. B, 122, 959
Fernandez-Soto A., Lanzetta K. M., Chen H.-W., 2003, MNRAS, 342, 1215
Ferrara A., Pettini M., Shchekinov Y., 2000, MNRAS, 319, 539
Finkelstein S. L., Rhoads J. E., Malhotra S., Pirzkal N., Wang J., 2007, ApJ, 660, 1023
Finkelstein S. L., Rhoads J. E., Malhotra S., Grogin N. A., 2009, ApJ, 691, 465
Fujita A., Martin C. L., Mac Low M.-M., Abel T., 2003, ApJ, 599, 50
Furlanetto S. R., Schaye J., Springel V., Hernquist L., 2005, ApJ, 622, 7
Gawiser E. et al., 2006, ApJ, 642, 13
Gnedin N. Y., Kravtsov A. V., Chen H. W., 2008, ApJ, 672, 765
Haiman Z., Cen R., 2005, ApJ, 623, 627
Iliev I. T., Shapiro P. R., McDonald P., Mellema G., Pen U.-L., 2008, MNRAS, 391, 63
Kashikawa N. et al., 2006, ApJ, 648, 7
Lai K., Huang J., Fazio G., Cowie L. L., Hu E. M., Kakazu Y., 2007, ApJ, 655, 704
Lai K. et al., 2008, ApJ, 674, 70
Leitherer C. et al., 1999, ApJS, 123, 3
Lisenfeld U., Ferrara A., 1998, ApJ, 496, 145
Mac Low M.-M., Ferrara A., 1999, ApJ, 513, 142
McKee C. F., 1989, Proc IAU Symp. 135, Interstellar Dust. Kluwer, Dordrecht, p. 431
McQuade K., Calzetti D., Kinney A. L., 1995, ApJS, 97, 331
McQuinn M., Hernquist L., Zaldarriaga M., Dutta S., 2007, MNRAS, 381, 75
Maiolino R. et al., 2006, Mem. Soc. Astron. Ital., 77, 643
Maiolino R. et al., 2008, A&A, 488, 463
Malhotra S., Rhoads J. E., 2004, ApJ, 617, 5
Malhotra S., Rhoads J. E., 2005, A&AS, 206, 2109
Malhotra S. et al., 2005, ApJ, 626, 666
Maselli A., Ferrara A., Ciardi B., 2003, MNRAS, 345, 379
Maselli A., Ciardi B., Kanekar A., 2009, MNRAS, 393, 171
Mesinger A., Furlanetto S. R., 2008, MNRAS, 386, 1990
Mesinger A., Haiman Z., Cen R., 2004, ApJ, 613, 23
Miralda-Escudé J., 1998, ApJ, 501, 15
Nagamine K., Ouchi M., Springel V., Hernquist L., 2008, preprint (arXiv:0802.0228)
Neufeld D. A., 1991, ApJ, 370, 85
Nozawa T., Kozasa T., Umeda H., Maeda K., Nomoto K., 2003, ApJ, 598, 785
Nozawa T., Kozasa T., Habe A., Dwek E., Umeda H., Tominaga N., Maeda K., Nomoto K., 2007, ApJ, 666, 955
Ono Y., Ouchi M., Shimasaku K., Dunlop J., Farrah D., McLure R., Okamura S., 2010, preprint (arXiv:1004.0963)
Osterbrock D. E., 1989, Astrophysics of Gaseous Nebulae and Active Galactic Nuclei. Univ. Sci. Books, Sausalito, CA
Ouchi M. et al., 2008, ApJS, 176, 301
Panter B., Jimenez R., Heavens A. F., Charlot S., 2008, MNRAS, 391, 1117
Peebles P. J. E., 1993, Principles of Physical Cosmology. Princeton Univ. Press, Princeton
Pirzkal N., Malhotra S., Rhoads J. E., Xu C., 2007, ApJ, 667, 49
Razumov A. O., Sommer-Larsen J., 2006, ApJ, 651, 89
Razumov A. O., Sommer-Larsen J., 2010, ApJ, 710, 1239
Ricotti M., Shull J. M., 2000, ApJ, 542, 548
Santos M. R., 2004, MNRAS, 349, 1137
Shimasaku K. et al., 2006, PASJ, 58, 313
Sokasian A., Abel T., Hernquist L S. V., 2003, MNRAS, 344, 607

Springel V., 2005, MNRAS, 364, 1105
Springel V., Herquist L., 2003, MNRAS, 339, 312
Steidel C. C., Pettini M., Adelberger K. L., 2001, ApJ, 546, 665
Storchi-Bergmann T., Kinney A. L., Challis P., 1995, ApJS, 98, 103
Stratta G., Maiolino R., Fiore F., D'Elia V., 2007, ApJ, 661, 9
Taniguchi Y. et al., 2005, PASJ, 57, 165
Todini P., Ferarra A., 2001, MNRAS, 325, 726

Tremonti C. A. et al., 2004, ApJ, 613, 898
Wise J. H., Cen R., 2009, ApJ, 693, 984
Yajima H., Choi J. H., Nagamine K., 2010, preprint (arXiv:1002.3346)
Zheng Z., Cen R., Trac H., Miralda-Escude J., 2010, ApJ, 716, 574

This paper has been typeset from a TEX/LATEX file prepared by the author.